

---

# FUSING PHYSICS-BASED AND DEEP LEARNING MODELS FOR PROGNOSTICS

---

A PREPRINT

**Manuel Arias Chao**  
ETH Zurich  
manuel.arias@ethz.ch

**Chetan Kulkarni**  
KBR, Inc., NASA Ames Research Center  
chetan.s.kulkarni@nasa.gov

**Kai Goebel**  
Luleå University of Technology  
kai.goebel@ltu.se

**Olga Fink**  
ETH Zurich  
ofink@ethz.ch

May 29, 2022

## ABSTRACT

Data-driven and physics-based models for remaining useful lifetime (RUL) prediction typically suffer from two major challenges that limit their applicability to complex real-world domains: (a) high complexity or incompleteness of physics-based models and (b) limited representativeness of the training dataset for data-driven models. The work proposed in the paper describes a novel hybrid framework for fusing the information from physics-based performance models with deep learning algorithms for prognostics of complex safety critical systems under real-world scenarios. In this framework, we use physics-based performance models to infer unobservable model parameters related to the system's components health solving a calibration problem a.k.a. an inverse problem. These parameters are subsequently combined with sensor readings and used as input to a deep neural network to generate a data-driven prognostics model. The performance of the hybrid framework is evaluated on a synthetic dataset comprising run-to-failure degradation trajectories from a small fleet of nine turbofan engines under a wide range of real flight conditions. The dataset was generated with the Commercial Modular Aero-Propulsion System Simulation (C-MAPSS) dynamical model developed at NASA. The performance of the approach is compared to an alternative data-driven approach where only sensor data are used as input to the deep neural network. A scenario of incomplete representation of the test degradation conditions in the training dataset is evaluated. The experimental results show that the hybrid framework outperforms the alternative pure data-driven approach by extending the prediction horizon by nearly 100% and decreasing the prediction error by 34% based on the applied metrics.

**Keywords** prognostics, deep learning, hybrid, C-MAPSS

## 1 Introduction

The prediction of the failure time in complex systems has been traditionally addressed on the basis of models that capture the physics of failure. While extensive research on physics-based models has been performed [1, 2], physical degradation processes are only well-understood for critical or relatively simple components. For prognostics in large mechatronic systems with complex physics of failure, capturing the comprehensive interconnected relationship of components is difficult using an approach based on pure model-based techniques. As a result, fielded implementations of physics-based models in practical applications have been limited.

The increased availability of system condition monitoring data has triggered the desire to use data-driven approaches for prognostics and health management (PHM) of complex engineered systems. The underlying assumption of these approaches is that the relevant information on the evolution of the system health and the failure time can be learned from

past data [3]. In particular, deep learning has recently gained attention due to its ability to learn failure patterns directly from raw sensor data [4]. A variety of supervised and semi-supervised deep learning models have shown promising performance in estimating the RUL from sensor data [5, 6, 7, 8, 9] for various prognostics benchmark problems [10, 11]. However, most research studies on deep learning applications in PHM require a representative dataset of end-to-end (i.e. run-to-failure) degradation trajectories to obtain accurate prognostics models. These trajectories need to be comprised of a set of time series sensor readings along with the corresponding time-to-failure labels covering the possible expected system conditions and failure modes. However, the collection of a representative dataset for systems subjected to periodic maintenance interventions can take a long time as (a) failures may be rare and (b) the system can operate in different environments and follow different mission profiles resulting in a large range of possible deterioration trajectories. For these reasons, in real application scenarios, the available datasets contain generally only a small number of units and failure modes and are, therefore, not fully representative of all potential future degraded system conditions. Moreover, for complex engineered systems with substantial variability of operating conditions and continuously increasing degradation, data-driven approaches struggle to distinguish between the impact of changing operating conditions and the impact of degradation on the sensor readings. Consequently, data-driven methods have difficulties to relate the condition monitoring data to the asset failure time limiting their practical applications.

Although, data-driven and physics-based approaches have limitations when applied as stand-alone approaches, it is hypothesized that the combined use of data-driven and physics-based approaches, potentially lead to performance gains by leveraging the advantages of each method. In particular, while physics-based approaches are generally limited by their high complexity or incompleteness, they do not require large amounts of data, retain the interpretability of a model and can generate synthetic data. In contrast, data-driven approaches are limited by the representativeness of the training datasets but are simple to implement and are able to discover complex patterns from large volumes of data. It follows that data-driven solutions could be advantageous to enhance or replace inaccurate parts of the physics-based models. In addition, model information can help to reduce the need for abundant datasets by providing model parameters that are very informative. In general the physics-based system models can be used as 'teachers' to guide the discovery of meaningful machine learning models. Simulation models can be used, therefore, to overcome the lack of time-to-failure trajectories and can be used to generate synthetic data.

Different approaches have been proposed to combine physics-based and data-driven approaches. Depending on what type of information is processed and how the pieces of information are combined, different types of hybrid architectures can be created. Some examples of hybrid models for prognostics are [12, 13, 14, 15, 16, 17]. In particular, hybrid systems combining thermodynamic performance models and data-driven aging models have shown promising results on individual simpler systems such as lithium batteries [14]. Recently, several approaches of physics-guided machine learning have been proposed, where physical principles are used to inform the search of a physically meaningful and accurate machine learning model. The architecture proposed in [18], for example, enhances the input space to a data-driven system model with outputs from a physics-based system model. As a result, the dynamical behavior of the system could be approximated more accurately. In another variation of the physics-guided machine learning idea, a recurrent neural network (RNN) cell was modified to incorporate the information from the system model as an internal state of the RNN. A related idea was applied to a variety of prognostics problems, such as in [15, 16, 17]. However, the underlying hypothesis of this method is that the output of the physics-based model is informative of the degradation process and consequently of the failure time. However, this ignores the fact that no model is perfect and not all the model outputs are equally informative of the degradation process. Consequently, the direct use of a model output does not guarantee a gain of useful information for predicting RUL.

Contrary to the previously proposed hybrid architectures, the framework presented in this paper leverages inferred **unobserved virtual sensors** and **unobservable parameters** of physics-based system models closely related to the system health to enhance the input space to deep learning-based prognostics models. For the physics-based system models, we focus on thermodynamic performance models (OD models) that are generally available for design, control or performance evaluation of complex systems. These system models have typically a moderate computational load and yet are able to predict measured process variables (e.g. temperatures, pressures or rotational speeds) as well as global unmeasured system and sub-system performance (e.g. efficiencies and power) [19]. The proposed hybrid framework was applied in [19] to diagnostic problems and has demonstrated that thermodynamic performance models offer access to health-related model parameters that are more sensitive to failure signatures. In this paper, we extend the framework to the prediction of the remaining useful life. In the proposed framework, thermodynamic performance models are used to infer model parameters that are informative of the health condition and its evolution in time by solving a calibration problem. These parameters are subsequently combined with sensor readings and used as input to a deep neural network to generate a data-driven prognostics model.

The performance of the hybrid framework is evaluated on a synthetic dataset comprising a small fleet of nine turbofan engines with run-to-failure degradation trajectories exhibiting a high variability in operating conditions. A scenario of incomplete representation of the test degradation conditions in the training dataset is considered. The dataset was

generated with the Commercial Modular Aero-Propulsion System Simulation (C-MAPSS) dynamical model [20]. Real flight conditions as recorded on board of a commercial jet were taken as input to the C-MAPSS model [21]. The performance of the approach is compared to an alternative data-driven approach where only sensor data are used as input to the deep neural network. The proposed hybrid method outperforms the equivalent data-driven approach and provides superior results in RUL estimation under highly varying operating conditions and incomplete representation of the training dataset.

## 2 Proposed Framework: Deep Learning-Based Prognostics with Physics Inferred Inputs

Thermodynamic performance models with different levels of fidelity are typically used to design and control complex engineered systems which are represented mathematically as coupled systems of nonlinear equations. Following the nomenclature and the problem formulation introduced in [19], the inputs of the models are divided into scenario-descriptor operating conditions  $w$  and unobservable model parameters  $\theta$ . The outputs of the system model are estimates of the measured physical properties  $\hat{x}_s$  and unobserved properties  $\hat{x}_v$  that are not part of the condition monitoring signals (i.e., *virtual sensors*). The nonlinear performance model is denoted as

$$[\hat{x}_s, \hat{x}_v] = S(w, \theta) \quad (1)$$

The unobservable model parameters  $\theta$  of performance models correspond to tuning parameters generally related to the health condition of the sub-components of the system. Model calibration is an inverse problem that involves inferring the values of  $\theta$  that make the system response to reproduce the observations  $x_s$  as close as possible (i.e.  $\hat{x}_s \sim x_s$ ). Hence, as a system model degrades, model calibration provides estimates of the model parameters ( $\hat{\theta}$ ) that encode and explain the deteriorated behaviour of the sub-components. The resulting calibrated model i.e.,  $S(w, \hat{\theta})$  provides high confidence estimates of unobserved process variables  $\hat{x}_v$  that may be sensitive to fault signatures. Model calibration increases the amount of information available for developing a data-driven prognostics model. Therefore, we propose to enhance the input space of the data-driven prognostics model with the process variables  $[\hat{x}_s, \hat{x}_v, \hat{\theta}]$  inferred with the calibrated system performance model. To benefit from the learning ability of recent advances in deep learning, we propose to combine the physics-based performance models with deep learning architectures. Figure 1 shows a block diagram of the proposed calibration-based hybrid prognostics approach. The deep learning prognostics model receives scenario-descriptor operating conditions  $w$  and model variables  $[\hat{x}_s, \hat{x}_v, \hat{\theta}]$  as input. In contrast to a standard data-driven approach aiming to learn a mapping function from the CM signals to the RUL target  $y$  (i.e.,  $[w, x_s] \mapsto y$ ), we first obtain a more informative representation  $x$  with additional health related features inferred by calibration of a physics-based system model ( $[x_s, S(w, \cdot)] \mapsto \hat{\theta}$ ). In a second step, we find an optimal mapping  $\mathcal{G} : x \mapsto y$  from the enhanced input space  $x = [w, x_s, \hat{x}_s, \hat{x}_v, \hat{\theta}]$  to perform RUL estimation. The hybrid framework is very flexible and can be combined with any type of deep learning architectures. While in this research, we use feed-forward architectures, recurrent or convolutional structures may also be used.

The proposed hybrid methodology provides the following advantages compared to purely data-driven approaches:

- Ability to predict the remaining useful lifetime also when representative datasets to train data-driven approaches are sparse.
- Interpretability of the models and the corresponding outputs.
- Ability to generate additional run-to-failure trajectories to compensate for the lacking representativeness of the available condition monitoring data
- Robustness to sensor faults that can be distinguished against faulty conditions

## 3 Methods

### 3.1 Problem Formulation

The formulation of the prognostics problem addressed in this paper is formally introduced in the following. Given are multivariate time-series of condition monitoring sensors readings  $X_{s_i} = [x_{s_i}^{(1)}, \dots, x_{s_i}^{(m_i)}]^T$  and their corresponding RUL i.e.,  $Y_i = [y_i^1, \dots, y_i^{m_i}]^T$  from a fleet of  $N$  units ( $i = 1, \dots, N$ ). Each observation  $x_{s_i}^{(t)} \in R^p$  is a vector of  $p$  raw measurements taken at operating conditions  $w_i^{(t)} \in R^s$ . The length of the sensory signal for the  $i$ -th unit is given by  $m_i$ ; which can, in general, differ from unit to unit. The total combined length of the available data set is  $m = \sum_{i=1}^N m_i$ .

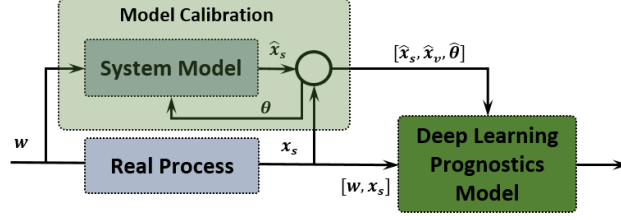


Figure 1: Overall architecture of the hybrid prognostics framework fusing physics-based and deep learning models. The deep learning prognostics model receives as input the scenario-descriptor operating conditions ( $w$ ), sensor readings ( $x_s$ ), estimates of the sensor readings ( $\hat{x}_s$ ) and the virtual sensors ( $\hat{x}_v$ ) and unobservable model parameters ( $\hat{\theta}$ ). The feedback arrow to the system model represents the calibration process for updating unobservable model parameters  $\theta$ .

More compactly, we denote the available dataset as  $\mathcal{D} = \{W_i, X_{s_i}, Y_i\}_{i=1}^N$ . In addition to the CM data and the RUL label, we have access to a system model  $S(w, \theta_{\text{ref}})$  which provides the expected dynamical response of a non-degraded reference unit (i.e.,  $\theta = \theta_{\text{ref}}$ ). Starting from an unknown initial health condition, the CM data of each unit records the degradation process of the system's components. The system's components experience *normal* (linear) degradation until point in time  $t_{s_i}$  where an *abnormal* condition arises leading to an eventual failure at  $t_{\text{EOL}_i}$  (end-of-life).

Given this set-up, the task is to obtain a predictive model  $\mathcal{G}$  that provides a reliable RUL estimate ( $\hat{Y}$ ) on a test dataset of  $M$  units  $\mathcal{D}_{T*} = \{X_{s_j*}\}_{j=1}^M$ ; where  $X_{s_j*} = [x_{s_j*}^1, \dots, x_{s_j*}^{k_j}]$  are multivariate time-series of sensors readings. The total combined length of the test data set is  $m_* = \sum_{j=1}^M k_j$ .

### 3.2 System Model Calibration

Inference of model parameters of computer models from observations  $x_s$  is often referred as a calibration [22]. System model calibration is an inverse problem aiming to obtain the values of the model parameters  $\theta$  that make the system response follows the observations i.e.,  $\hat{x}_s \sim x_s$ . Since both, the measurement data and model parameters, are uncertain, the process of estimating optimal correcting parameters is a stochastic calibration problem [23]. Ideally, the calibration process aims at obtaining the posterior distribution of the calibration factors given the data  $p(\theta|w, x_s)$ . However, computing the whole distribution is generally computationally expensive and, therefore, in most cases, point value estimations of the parameters are inferred. A typical compromise is to compute the *maximum a posteriori estimation* (MAP), described by

$$\hat{\theta}_{\text{MAP}} = \arg \max_{\theta} p(\theta|w, x_s) \quad (2)$$

Several calibration methods have been proposed and the large majority of the developed methods can be classified as probabilistic matching approaches [24]. Some of the most commonly used calibration approaches include weighted linear and non-linear least squares schemes, maximum likelihood estimates, Bayesian inference methods (e.g. Markov Chain Monte Carlo, Particle and Kalman filters) [22, 25, 26, 27]. These methods differ in the level of complexity and the computational cost.

In this work, rather than focusing on one particular model calibration method, we are aiming at presenting and demonstrating the benefit of combining physics-inferred model parameters representing sub-model health with deep learning models to generate accurate prognostics models. Furthermore, the goal is to evaluate the impact of different levels of calibration accuracy on the performance of the proposed prognostics framework. Since the calibration of the performance model itself is not in the focus of this research, we apply a state-of-the-art approach for calibration: an Unscented Kalman Filter [28] to infer the values of the model correcting parameters  $\theta$ . The rationale for this choice is that our models of interest are nonlinear and that UKF provides a good compromise between computational cost and performance. In fact, UKF is widely applied for aircraft engines health evaluation [25, 26, 19]. However, we would like to stress that the calibration task can be also performed with any other approach. The proposed framework is flexible with respect to the chosen model calibration approach.

Model-based estimation of the sub-model health parameters from a transient data stream can be addressed with a traditional state-space formulation. In particular, we consider a UKF where the state vector comprises the health parameters. The measurement equation depends on the states and the input signals at the present time step  $t$ . The measurement equation is readily available from the system model  $S$ . Hence, we consider a nonlinear discrete time

system of the form:

$$\theta^{(t)} = \theta^{(t-1)} + \xi^{(t)} \quad (3)$$

$$x_s^{(t)} = S(w^{(t)}, \theta^{(t)}) + \epsilon^{(t)} \quad (4)$$

where  $\xi \sim N(0, Q)$  is a Gaussian noise with covariance  $Q$  and  $\epsilon \sim N(0, R)$  is a Gaussian noise with covariance  $R$ . A more detailed explanation of this problem formulation applied to the monitoring of gas turbine engines can be found in [26].

It is worth pointing out that the proposed formulation of the calibration problem assumes that deviation of the system model response and the true system response is rooted in an inaccurate but complete representation of the real physical process. In other words, there isn't any substantial missing physical representation of the dynamic system  $S$  that would make the model  $S(w, \theta)$  unable to reproduce the true system response closely for some unknown  $\hat{\theta}$ . This is a common situation when considering system models of critical systems and mature products where the system model has been developed and validated based on multiple field units or test bed units. In contrast, this is, typically, not the case for new developments. In general, a certain level of missing physical representation on the system model will result in a lower calibration quality. In case of significant missing physics within the system model representation, the impact of model degradation gets entangled with the model correction rooted in the lack of a physics-based model. Model calibration under this scenario is an open research question that we do not address in this article.

### 3.3 Deep Learning-Based Prognostics with Physics Inferred Inputs

The inferred model parameters  $\hat{\theta}$  are informative about the health state of the system but do not provide a direct relation to the end-of-life time. Together with the scenario-descriptor operating conditions  $w$ , they comprise the 'expected' independent factors of variation of sensor readings ( $X_s$ ). Consequently, the inferred model parameters  $\hat{\theta}$  are ideal parameters to disentangle the contribution of system degradation and operation condition change  $w$  from the observed system responses. Based on this reasoning, the model correcting parameters are the perfect complement to the raw sensor readings for the generation of data-driven prognostics models.

Since deep learning models have shown an excellent ability to reveal hidden complex functional mapping between inputs and target labels, we choose a deep neural network to discover a mapping  $\mathcal{G}$  that relates the enhanced input  $X = [W, X_s, \hat{X}_s, \hat{X}_v, \hat{\theta}]$  to a target label  $\mathbf{Y}$  given a training set  $S_T \subset \mathcal{D}$ . Again, multiple learning strategies are possible for this task (supervised or semi-supervised learning). In this research, we chose the standard supervised learning strategy (SL) i.e., a direct mapping from input  $\mathbf{X}$  to a target label  $\mathbf{Y}$ . The main reasons for this choice are the simplicity and suitability to the problem formulation in Section 3.1. It should be pointed out that under a slightly different problem formulation, a semi-supervised learning or a domain adaptation strategy could be also potentially applied. To obtain the mapping function  $\mathcal{G}$ , a deep feed-forward neural network (FF) is evaluated within the proposed framework. As already mentioned earlier, different types of architectures, including also recurrent structures, could be used within the proposed framework. Section 4.3 provides further details about the architecture. The entire procedure proposed in this paper is summarized in Algorithm 1.

## 4 Case Study

### 4.1 A Small Fleet of Turbofan Engines

The proposed methodology is demonstrated and evaluated on a synthetic dataset with run-to-failure degradation trajectories of a small fleet comprising nine turbofan engines with unknown and different initial health conditions. The dataset was generated with the Commercial Modular Aero-Propulsion System Simulation (C-MAPSS) dynamical model [20]. Real flight conditions as recorded on board of a commercial jet were taken as input to the C-MAPSS model [21]. Figure 2 shows the kernel density estimations of the simulated flight envelopes given by the scenario-descriptor variables  $W$ : altitude (alt), flight Mach number (XM), throttle-resolver angle (TRA) and total temperature at the fan inlet (T2) for  $N = 6$  training units ( $u = 2, 5, 10, 16, 18$  &  $20$ ) and  $M = 3$  test units ( $u = 11, 14$  &  $15$ ). It is worth noticing that test units 14 and 15 have an operation distribution that is significantly different from training units. Concretely, test units 14 and 15 operate shorter and lower altitude flights compared to other units. The training dataset, therefore, contains flight profiles that are not fully representative for the test conditions of these two units. We have chosen this example due to its relevance for practical applications where observed operating conditions of new units may not correspond to the past operating conditions of other units in the fleet. Pure data-driven approaches generally require domain-adaptation approaches for this type of setup [29].



**Algorithm 1:** Calibration-based Hybrid Deep Learning Prognostics

---

**Input:**  $\{w^{(i)}, x_s^{(i)}\}_{i=1}^m \in \mathcal{D}$  &  $S(w^{(t)}, \theta_{\text{ref}})$   
**for**  $i = 1 : m$  **do**  
   $\hat{\theta}^{(i)} \leftarrow \arg \max_{\theta} p(\theta^{(i)} | (w^{(i)}, x_s^{(i)}))$   
**end**  
**Input:**  $\{w^{(i)}, x_s^{(i)}, \hat{x}_s^{(i)}, \hat{x}_v^{(i)}, \hat{\theta}^{(i)}, y^{(i)}\}_{i=1}^{m_{ST}} \in S_T$   
 $X = \{w^{(i)}, x_s^{(i)}, \hat{x}_s^{(i)}, \hat{x}_v^{(i)}, \hat{\theta}^{(i)}\}_{i=1}^{m_{ST}}$  Enhanced Input - $X$   $\mathcal{H} \leftarrow$  Initialize parameters in Prognostics Network  
**while**  $i \leq E_s$  **do**  
   $\mathcal{H} \leftarrow$  Update parameters using SGD  
**end**  
**Input:**  $\{w_*^{(j)}, x_{s*}^{(j)}\}_{j=1}^{m_*} \in \mathcal{D}_{T*}$  &  $S(w^{(t)}, \theta_{\text{ref}})$   
**for**  $j = 1 : m_*$  **do**  
   $\hat{\theta}_*^{(j)} \leftarrow \arg \max_{\theta} p(\theta^{(j)} | (w_*^{(j)}, x_{s*}^{(j)}))$   
**end**  
**Input:**  $\{w_*^{(j)}, x_{s*}^{(j)}, \hat{x}_{s*}^{(j)}, \hat{x}_{v*}^{(j)}, \hat{\theta}_*^{(j)}\}_{j=1}^{m_*} \in D_T$   
 $X_* = \{w_*^{(j)}, x_{s*}^{(j)}, \hat{x}_{s*}^{(j)}, \hat{x}_{v*}^{(j)}, \hat{\theta}_*^{(j)}\}_{j=1}^{m_*}$  Enhanced Input - $X_*$   
**for**  $j = 1 : m_*$  **do**  
   $\hat{y}^{(j)} \sim \mathcal{G}(x_*^{(j)}; \mathcal{H})$   
**end**

---

An example of a typical single flight cycle given by traces of the scenario-descriptor variables is shown in Figure 3. Each flight cycle contains recordings of varying lengths, covering climb, cruise and descend flight conditions (with alt > 10000 ft) corresponding to different flight routes operated by the aircraft. The remaining units of the fleet follow similar flight traces.

Two distinctive failure modes are present in the available dataset ( $\mathcal{D}$ ). Units 2, 5 and 10 have failure modes of an *abnormal* high pressure turbine (HPT) efficiency degradation. Units 16, 18 and 20 are subject to a more complex failure mode that affects the low pressure turbine (LPT) efficiency and flow in combination with the high pressure turbine (HPT) efficiency degradation. Test units are subjected to the same complex failure mode. Figure 4 shows degradation profiles induced in the nine units of the fleet. The initial deterioration of each unit is different and corresponds to an engine-to-engine variability equivalent to a 10% of the health index. The degradation of the affected system components follows a stochastic process with a linear *normal degradation* followed by a steeper *abnormal degradation*. The degradation rate of each component varies within the fleet. The transition from *normal* to *abnormal* degradation is smooth and occurs at different cycle times for each unit. The transition time ( $t_s$ ) is dependent on the operating condition i.e., flight and degradation profile. It should be noted that although the degradation profiles of individual components show nearly overlapping trajectories, the combined profile i.e., the profile in the three dimensions is clearly different. More details about the generation process can be found in [30].

An overview of the transition times  $t_s$ , the end-of-life times  $t_{EOL}$  and the number of samples from each unit of the fleet  $m_i$  is provided in Table 1. The sampling rate of the data is 1Hz resulting in a total size of the dataset of 5.3M samples for training and 1.2M samples for testing. It is worth noticing that while test unit 14 is a short flight engine with the lowest amount of flight time (0.16M seconds) it has the largest number of flight cycles.

In addition to the CM data we have access to a system model  $S(w, \theta_{\text{ref}})$  (i.e., C-MAPSS dynamical model) which provides the expected dynamical response of a non-degraded reference unit ( $\theta = \theta_{\text{ref}}$ ). It is worth noticing that this reference system response deviates from the responses of each of the units due to the different initial health condition and the degradation trajectories experienced by each unit.

## 4.2 Pre-processing

The dimension of the input space  $n$  ( $X \in R^{m \times n}$ ) varies depending on the selected solution strategy (see Table 2). The data-driven model based only on condition monitoring signals have 18 inputs. The proposed hybrid method has 30 inputs (including additionally the model calibration parameters and the virtual sensors). Tables 3 to 5 provide a detailed overview of the model variables included in the condition monitoring signals  $[W, X_s]$ , virtual sensors  $\hat{X}_v$  and model

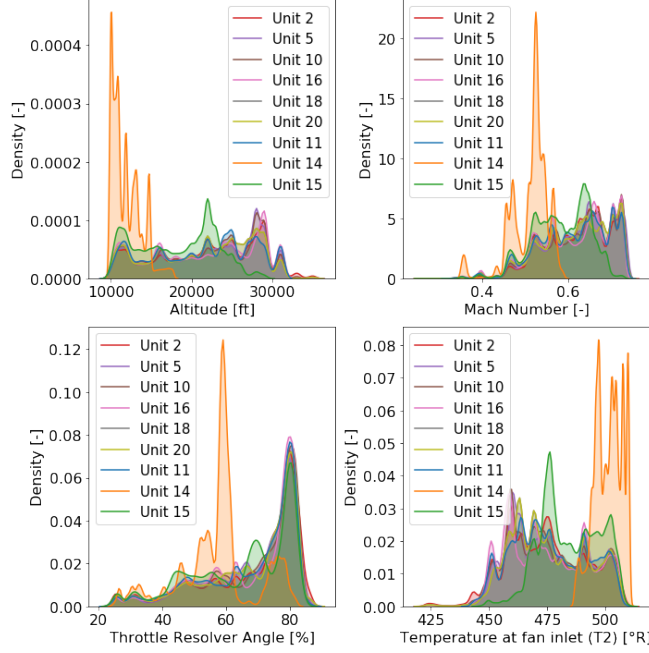


Figure 2: Kernel density estimations of the simulated flight envelopes given by recordings of altitude, flight Mach number, throttle-resolver angle (TRA) and total temperature at the fan inlet (T2). The complete run-to-failure trajectories of nine fleet units are shown.  $N = 6$  training units ( $u = 2, 5, 10, 16, 18$  &  $20$ ) and  $M = 3$  test units ( $u = 11, 14$  &  $15$ ) are represented. Test Unit 11 (blue) has a similar operation profile as the training units. Test units 14 (orange) and Unit 15 (green) operate shorter and lower altitude flights.

Available Dataset - $\mathcal{D}$				
Unit ( $u$ )	$m_i$	$t_s$	$t_{EOL}$	Failure Mode
2	0.85M	17	75	HPT
5	1.03M	17	89	HPT
10	0.95M	17	82	HPT
16	0.77M	16	63	HPT+LPT
18	0.89M	17	71	HPT+LPT
20	0.77M	17	66	HPT+LPT
Test Dataset - $\mathcal{D}_{T*}$				
Unit ( $u$ )	$m_j$	$t_s$	$t_{EOL}$	Failure Mode
11	0.66M	19	59	HPT+LPT
14	0.16M	36	76	HPT+LPT
15	0.43M	24	67	HPT+LPT

Table 1: Size ( $m_u$ ), the transition cycle time ( $t_s$ ) and end-of-life time ( $t_{EOL}$ ) of each unit within the available ( $\mathcal{D}$ ) and test datasets ( $\mathcal{D}_{T*}$ ).

parameters  $\hat{\theta}$ . The variable name corresponds to the internal variable name used in CMAPSS. The descriptions and units are reported as provided in the model documentation [20].

The input space  $X$  to the models is normalized to a range  $[-1, 1]$  by a min/max-normalization given the available dataset ( $\mathcal{D}$ ). A validation set  $V_T \subset \mathcal{D}$  comprising 10 % of the available data was chosen for hyperparameter model selection of the deep learning prognostics model.

### 4.3 Deep Learning Prognostics Model

As mentioned earlier, the main goal of this research study is to demonstrate the capability of the framework to perform prognostics with high accuracy and compare the proposed framework to purely data-driven and model-based

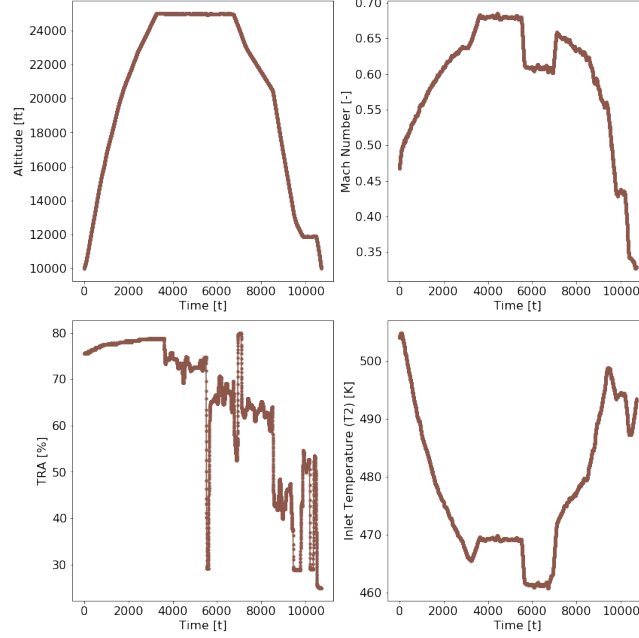


Figure 3: Single flight traces of altitude, flight Mach number (XM), throttle-resolver angle (TRA) and total temperature at the fan inlet (T2) for Unit 10. Climb, cruise and descend flight conditions (alt > 10000 ft) are covered.

Model Type	Input $X$	$n$
Data-Driven	$[W, X_s]$	18
Hybrid	$[W, X_s, \hat{X}_v, \hat{\theta}]$	30

Table 2: Overview of the input space dimensions ( $n$ ) for purely data-driven and hybrid approaches.

approaches. To evaluate the two approaches in a fair way, we consider a state-of-the-art deep neural network with a common architecture for the hybrid and the pure data-driven approach.

The end-of-life time of a mechanical system is typically related to the existence of a health index (HI). The health index is typically defined as a normalized margin to multiple health related thresholds evaluated at defined reference conditions. The end-of-life time of a mechanical system corresponds to the point in time where  $HI = 0$ . Under this definition, the health index is time independent and consequently, a time independent mapping from CM data and  $\hat{\theta}$  to HI exists. Therefore, it is theoretically possible to find a good mapping between the system state and the end of life based on feed forward network, in particular if abundant data are available. This theoretical possibility does not contradict the fact that the temporal information should enable more accurate predictions.

The proposed case study represents a time evolving process where the system response has factors of variation with varying operational dynamics. On the one hand, there is the fast response of the model to the flight conditions and control set-points (i.e  $w$ ) which follows the dynamics of  $< 1s$ . On the other hand, there is a slow degradation of the system component with dynamics in the order of the length of a flight (in this case, ranging from 1-10 hours). These different dynamics hinder the development of time-dependent deep learning models. In their basic form, deep learning models based on Recurrent Neural Networks (RNN) or Convolutional Neural networks (CNN) resort to a fixed time window size that will not be able to capture these two very different dynamics in the time series. Modifications of the standard RNN or CNN frameworks to capture very different time scales is a current research topic that is not addressed in this work.

Following these two arguments, in the proposed approach here, we selected a deep feed-forward neural network for the generation of the deep learning prognostics model.

**Network architecture.** The architecture of the feed-forward neural network used in this research comprises four fully connected layers ( $L = 4$ ). The three hidden layers have 100 neurons each ( $n^1 = n^2 = n^3 = 100$ ). In the final layer, a linear output neuron ( $n^L = 1$ ) was used. In compact notation, we refer to this architecture as  $[n, 100, 100, 100, 1]$ , where  $n$  denotes the size of the input space  $X$  and can vary depending on the considered solution strategy (see Table 2).



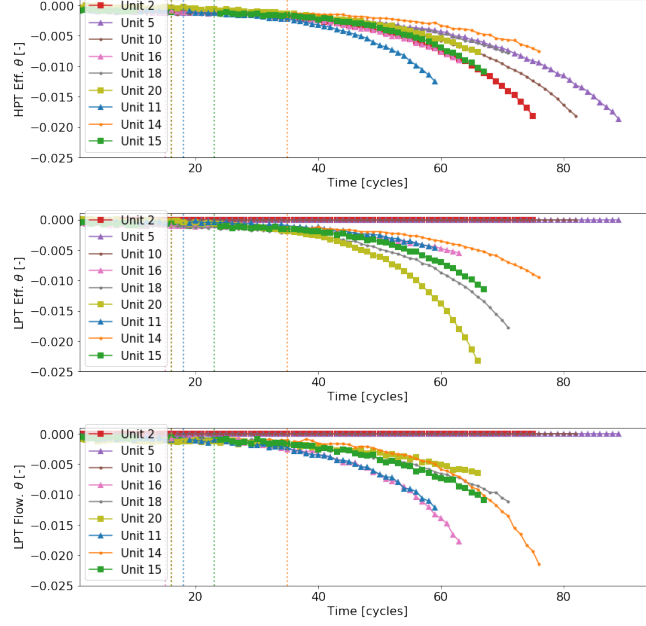


Figure 4: Traces of the degradation imposed on the high pressure turbine efficiency (HPT\_Eff\_mod), low pressure turbine efficiency (LPT\_Eff\_mod) and low pressure turbine flow (LPT\_flow\_mod) for each unit of the fleet. The onset of the abnormal degradation (i.e.  $t_s$ ) of each unit is indicated by dashed vertical lines.

#	Symbol	Description	Units
1	alt	Altitude	ft
2	XM	Flight Mach number	-
3	TRA	Throttle-resolver angle	%
4	Wf	Fuel flow	pps
5	Nf	Physical fan speed	rpm
6	Nc	Physical core speed	rpm
7	T2	Total temperature at fan inlet	°R
8	T24	Total temperature at LPC outlet	°R
9	T30	Total temperature at HPC outlet	°R
10	T48	Total temperature at HPT outlet	°R
11	T50	Total temperature at LPT outlet	°R
12	P15	Total pressure in bypass-duct	psia
13	P2	Total pressure at fan inlet	psia
14	P21	Total pressure at fan outlet	psia
15	P24	Total pressure at LPC outlet	psia
16	Ps30	Static pressure at HPC outlet	psia
17	P40	Total pressure at burner outlet	psia
18	P50	Total pressure at LPT outlet	psia

Table 3: Condition monitoring signals -  $[w, x_s]$ . The variable symbol corresponds to the internal variable name in CMAPSS. The descriptions and units are reported as in the model documentation [20].

*ReLU* activation function was used throughout the entire network. It should be noted that RUL estimation problem is a regression problem. Therefore, the last activation  $\sigma^L = I$  is the identity. Figure 5 shows the resulting network architecture. The network has 24k trainable parameters ( $\mathcal{H}$ ).

#	Name	Description	Units
19	T40	Total temp. at burner outlet	°R
20	P30	Total pressure at HPC outlet	psia

Table 4: Virtual sensors -  $[x_v]$ . The variable symbol corresponds to the internal variable name in CMAPSS. The descriptions and units are reported as in the model documentation [20].

#	Symbol	Description	Units
21	fan_eff_mod	Fan efficiency modifier	-
22	fan_flow_mod	Fan flow modifier	-
23	LPC_eff_mod	LPC efficiency modifier	-
24	LPC_flow_mod	LPC flow modifier	-
25	HPC_eff_mod	HPC efficiency modifier	-
26	HPC_flow_mod	HPC flow modifier	-
27	HPT_eff_mod	HPT efficiency modifier	-
28	HPT_flow_mod	HPT flow modifier	-
29	LPT_eff_mod	LPT efficiency modifier	-
30	LPT_flow_mod	HPT flow modifier	-

Table 5: Model correcting parameters -  $[\theta]$ . The variable symbol corresponds to the internal variable name in CMAPSS. The descriptions and units are reported as in the model documentation [20].

#### 4.4 Training Set-up

The optimization of the network’s weights was carried out with mini-batch stochastic gradient descent (SGD) and with the *Adam* algorithm [31]. *Xavier* initializer [32] was used for the weight initializations. The batch size was set to 1024 and the learning rate to 0.001. The number of epochs ( $E_s$ ) was set to 200.

#### 4.5 Evaluation Metrics

The performance of the proposed method is evaluated and compared to alternative deep learning models on the selected prognostics task. We define two common evaluation metrics in C-MAPSS prognostics analysis: root-mean-square error (RMSE) and NASA’s scoring function [33] ( $s$ ) which are defined as:

$$s = \sum_{j=1}^{m_*} \exp(\alpha |\Delta^{(j)}|) \quad (5)$$

$$RMSE = \sqrt{\frac{1}{m_*} \sum_{j=1}^{m_*} (\Delta^{(j)})^2} \quad (6)$$

where  $m_*$  denotes the total number of test data samples,  $\Delta^{(j)}$  is the difference between the estimated and the real RUL of the  $j$  sample (i.e.  $y^{(j)} - \hat{y}^{(j)}$ ) and  $\alpha$  is  $\frac{1}{13}$  if RUL is under-estimated and  $\frac{1}{10}$  otherwise. The resulting  $s$  metric is not symmetric and penalizes over-estimation more than under-estimation.

Unit specific point-wise RUL estimation (i.e.  $\hat{y}_u^{(j)}$ ) can show a high variability within a flight cycle, indicating that some parts of the flight are more informative for RUL estimation compared to other parts. In order to evaluate this effect we also define average RUL estimation at cycle  $c$  in unit  $u$  ( $\hat{y}_u^{[c]}$ ) which is defined as follows:

$$\hat{y}_u^{[c]} = \frac{1}{m_u^{[c]}} \sum_{j=1}^{m_u^{[c]}} y_u^{(j)} \quad (7)$$

where  $m_u^{[c]}$  is the length of the flight cycle  $c$  for the  $u$ -th unit; which is formally defined using the indicator function i.e.  $\mathbf{1}\{\cdot\}$  as:

$$m_u^{[c]} = \sum_{j=1}^{m_*} \mathbf{1}\{U^{(j)} = u \wedge C^{(j)} = c\} \quad (8)$$

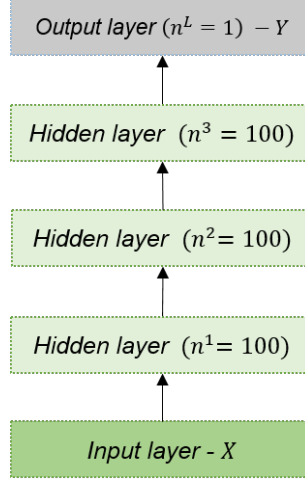


Figure 5: SL-FF model.  $n^l$  denotes the dimension at the each layer (i.e. number of neurons).

where  $U$  and  $C$  are vectors with unit and cycle labels for each sample of the test dataset.

Contrary to the original C-MAPSS dataset [33], in this analysis, we have access to the complete run-to-failure trajectory of the test units. Therefore, to evaluate the model performance at different points of time ( $c$ ) we compute the values of  $s$  and  $RMSE$  at intermediate points in time  $c$ . We define, therefore, the average prognostics score of the  $u$ -th unit at cycle  $c$  ( $s_u^{[c]}$ ). In other words, we compute the expected RUL given *partial* degradation trajectories containing all the time steps preceding flight cycle  $c$ . The resulting metric is given by the following expression:

$$s_u^{[\leq c]} = \frac{1}{m_u^{[\leq c]}} \sum_{j=1}^{m_u^{[\leq c]}} \exp(\alpha |y_u^{(j)} - \hat{y}_u^{(j)}|) \quad (9)$$

$$RMSE_u^{[\leq c]} = \sqrt{\frac{1}{m_u^{[\leq c]}} \sum_{j=1}^{m_u^{[\leq c]}} (y_u^{(j)} - \hat{y}_u^{(j)})^2} \quad (10)$$

where  $m_u^{[\leq c]}$  is the number of sample points from past flights at flight cycle  $c$  for the  $u$ -th unit; which is formally defined using the indicator function  $\mathbf{1}\{\cdot\}$  as:

$$m_u^{[\leq c]} = \sum_{j=1}^{m_*} \mathbf{1}\{U^{(j)} = u \wedge C^{(j)} \leq c\} \quad (11)$$

## 5 Experimental Results

### 5.1 Model Calibration

As described above, the calibration was performed with UKF. Figure 6 exemplarily shows the inferred unobserved model parameters  $\hat{\theta}$  obtained for Unit 11 with the state-space formulation introduced in Section 3.3. The calibration process is time intensive. Therefore, we limited the number of points per cycle to three randomly selected points within each flight envelope. Since the degradation of the system is only noticeable between flights and it is assumed to be constant throughout each cycle, this simplification is well-founded. It is observed that after 10 operation cycles, the Unscented Kalman Filter converges and is able to accurately identify and track degradation of the three calibration factors affected by the simulated failure mode. The UKF performance on other test or training units shows similar results.

### 5.2 RUL Estimation

The RUL estimation is performed based on the same feed-forward neural network architecture for both setups: the purely data-driven and the proposed hybrid approach. In the following, the performance of the two approaches is

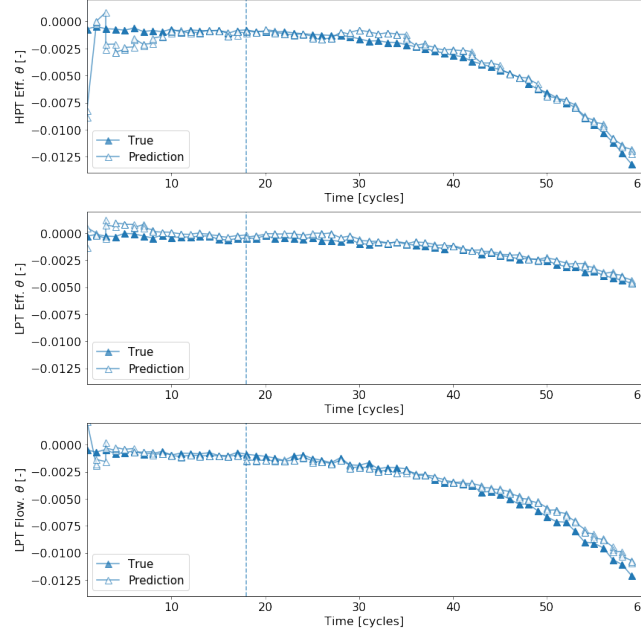


Figure 6: True (blue triangles) and predicted (white triangles) traces of HPT efficiency, LPT efficiency and flow scalars for the run-to-failure trajectory of Unit 11 with the UKF. The onset of the abnormal degradation ( $t_{s_u}$ ) is indicated with dashed vertical line.

Metric	Hybrid	Data-Driven	ref. Delta
RMSE [-]	<b>4.89</b>	7.45	-34%
$s \times 10^5$ [-]	<b>0.69</b>	1.30	-47%

Table 6: Overview of the RMSE and  $s$ -score metrics with hybrid and baseline approaches for complete degradation trajectories on testset ( $\mathcal{D}_{T*}$ ), comprising data from the three test units.

compared based on different metrics and with different time horizons. Table 6 shows the performance of failure time prediction of the proposed hybrid approach ( $X = [W, X_s, \hat{X}_v, \hat{\theta}]$ ) and the *baseline* approach (pure data-driven with  $X = [W, X_s]$ ). With a reduction of -34% in RMSE and -47% in  $s$  score the hybrid approach clearly outperforms the *baseline*. Since the  $s$ -score penalizes more over-estimation than under-estimation and RMSE is a symmetric metric, the greater reduction of  $s$  compared to RMSE indicates that the proposed method handles RUL over-estimation more effectively.

The metrics of RMSE and  $s$  score can also be evaluated on incomplete degradation trajectories of arbitrary lengths. Figure 7 shows the values of RMSE and  $s$  for degradation trajectories of  $c$  cycles i.e.,  $s^{[\leq c]}$  and  $RMSE^{[\leq c]}$ . For any given degradation trajectory with length  $c \geq 10$  cycles, the hybrid approach (bottom) leads to lower and more stable values of  $s^{[\leq c]}$  and  $RMSE^{[\leq c]}$  than the *baseline* (top). We conclude that the hybrid approach provides, therefore, overall the best prognostics performance at any point in time. The improvement in prognostics performance is also observed for individual test units. Figure 8 shows the true and predicted  $RUL$  of the *baseline* approach (top) and the proposed hybrid approach (bottom) for each of the test units. The full lines correspond to the true  $RUL$  i.e.  $y_u^{[c]}$ , the dots are the average  $RUL$  estimate at each cycle i.e.  $\hat{y}_u^{[c]}$  and the shaded surface shows the variability of the  $RUL$  predictions within each cycle. The upper limit corresponds to  $\max(\hat{y}_u^{[c]})$  and the lower bound to  $\min(\hat{y}_u^{[c]})$ .  $RUL$  estimates with the *baseline* approach at any point in time have a large variability and high bias (specifically,  $RUL$  over estimation) compared to the hybrid approach. Figure 9 shows in more detail the bias by representing the error of the average  $RUL$  prediction ( $\epsilon_{y_u} = \hat{y}_u^{[c]} - y_u^{[c]}$ ) for each unit. We can observe that the cycle time where  $|\epsilon_{y_u}|$  is below 5 cycles for any future time ( $t \geq c$ ) decreases for all the test units. We denote this time as  $t_{|\epsilon_{y_u}| \leq 5}$ . Table 7 reports the values of  $t_{|\epsilon_{y_u}| \leq 5}$  for each unit and whole fleet. The hybrid approach decreases the time for accurate prediction an average of 18 cycles which corresponds to an improvement of -39%. Table 7 also shows the improvements in the  $RUL$  prediction quantified

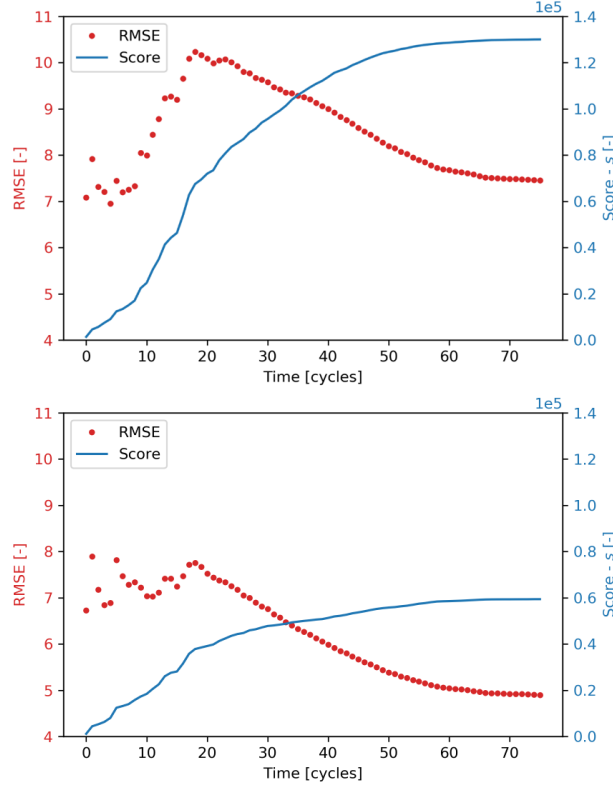


Figure 7: RUL prediction performance with incomplete degradation trajectories  $s^{[\leq c]}$  (blue) and  $RMSE^{[\leq c]}$  (red) with the *baseline* (top) and *hybrid* (bottom) approaches.

relative to  $t_{EOL}$ , i.e.,  $t_{EOL} - t_{\epsilon_y \leq 5}$ . Under this metric the proposed hybrid method provides an average 98% increase on the prediction horizon while maintaining a similar prediction accuracy.

$t_{\epsilon_y \leq 5}$ in [cycles]			
$u$	Hybrid	Data-Driven	rel.Delta
11	<b>28</b>	40	-30%
14	<b>32</b>	60	-47%
15	<b>29</b>	45	-36%
Fleet Avg.	<b>30</b>	48	-39%
$t_{EOL} - t_{\epsilon_y \leq 5}$ in [cycles]			
$u$	Hybrid	Data-Driven	rel.Delta
11	<b>31</b>	40	63%
14	<b>44</b>	60	175%
15	<b>38</b>	16	73%
Fleet Avg.	<b>38</b>	19	98%

Table 7: Overview of the prediction time [cycles] for  $\epsilon_y \leq 5$  with data-driven and hybrid approaches.

The quality of the calibration process has an impact on the prognostic performance. In order to quantify this impact, noise of different signal-to-noise ratios SNR are imposed on the calibration factors. We limited the noise perturbation to the three calibration factors that define the failure modes (i.e., *HPT\_Eff\_mod*, *LPT\_Eff\_mod* and *LPT\_Flow\_mod*). Figure 10 shows the resulting noisy calibration process  $\hat{\theta}$ . Table 8 reports the impact in RMSE and  $s$  of the three SNR evaluated values. We can observe a decrease in the accuracy as the noise increases for all the tested models. However, the proposed hybrid method is able to achieve a prognostics performance clearly above the purely data-driven models

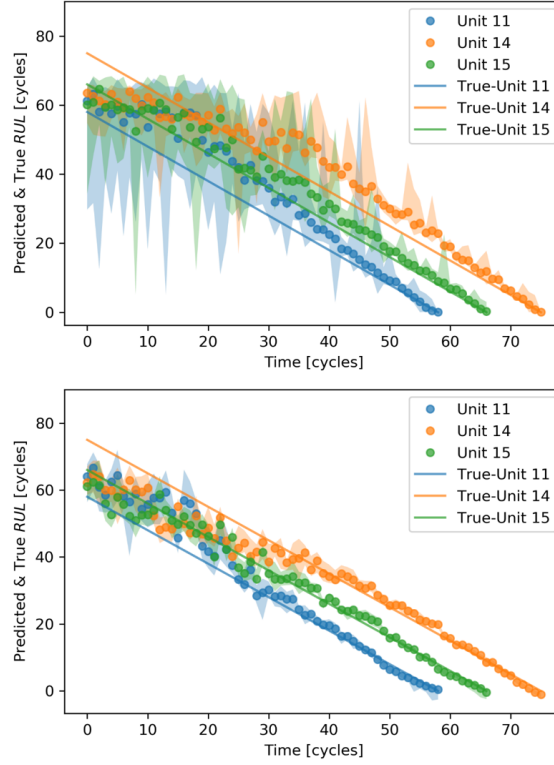


Figure 8: True and predicted *RUL* of the baseline model (top) and the proposed hybrid approach (bottom) for each test unit. The solid lines correspond to the true *RUL* i.e.  $y_u^{[c]}$ , the dotted lines are the average *RUL* estimate at each cycle i.e.  $\hat{y}_u^{[c]}$  and the shaded surface is the uncertainty bounds for *RUL* predictions within each cycle. The upper limit corresponds to  $\max(\hat{y}_u^{[c]})$  and the lower bound is  $\min(\hat{y}_u^{[c]})$ . The three test units are shown: unit 11 (blue), unit 14 (orange) and unit 15 (green).

Hybrid $X = [W, X_s, X_v, \hat{\theta}]$		
Intensity	RMSE [-]	$s \times 10^5$
$\text{SNR}_{db} = \infty$	<b>4.89</b>	<b>0.69</b>
$\text{SNR}_{db} = 30$	5.63	0.76
$\text{SNR}_{db} = 20$	6.05	0.85
$\text{SNR}_{db} = 10$	6.20	0.92
Data-Driven $X = [W, X_s]$		
Intensity	RMSE [-]	$s \times 10^5$
$\text{SNR}_{db} = \infty$	7.45	1.30

Table 8: Overview of the RMSE and  $s$  score results with hybrid and baseline approach

within all the evaluated SNR. Therefore, these results demonstrate the robustness of the proposed hybrid prognostics approach. Figure 11 shows in more detail the impact of noisy calibration on the prognostics performance of each unit. It should be noted that the  $\text{SNR}_{db}$  scale is logarithmic.

## 6 Conclusions

The work presented in this paper proposes a hybrid framework fusing information from the physics-based performance models with deep learning algorithms for prognostics of complex critical systems. Health related model parameters are



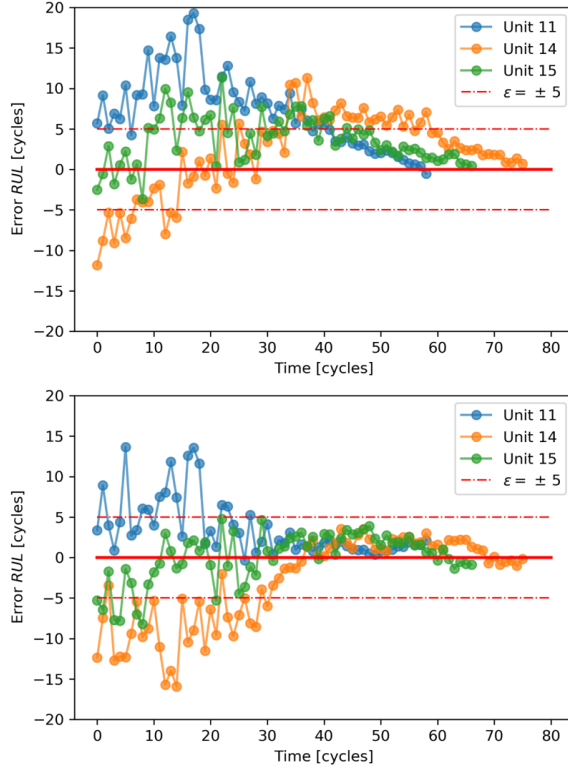


Figure 9: Average RUL prediction error ( $\epsilon_{y_u} = \hat{y}_u^{[c]} - y_u^{[c]}$ ) for each unit. The red dashed horizontal lines correspond to  $\pm 5$  cycles error bars. The three test units are shown: Unit 11 (blue), Units 14 (orange) and Unit 15 (green).

inferred by solving a calibration problem. Subsequently, this information is combined with sensor readings and used as input to a deep neural network to develop a reliable hybrid prognostics model.

The performance of the hybrid framework was evaluated on a synthetic dataset comprising run-to-failure degradation trajectories from a small fleet of nine turbofan engines operating under a large range of real flight conditions. The dataset was generated with the Commercial Modular Aero-Propulsion System Simulation (C-MAPSS) dynamical model. The proposed hybrid framework clearly outperforms the alternative data-driven prognostic model where only sensor data are used as input to the deep neural network. It provides accurate and robust predictions of the failure time,  $t_{EOL}$  (i.e.  $\epsilon \pm 5$  cycles) while extending the prediction horizon by nearly 100% compared to the pure data-driven methods.

As demonstrated in the experiments, the performance of the proposed hybrid prognostics framework is dependent on the quality of the calibration. However, its impact is moderate. If the calibrated system model fails to reproduce the real system response as a result of an incomplete physical representation of the system model or a poor performance of the chosen calibration method, the capability to infer relevant health information will consequently decrease affecting the prognostics performance. However, it is expected that the learning capabilities of the deep neural networks will be able to partially compensate for this.

This research study demonstrated the capabilities of the developed hybrid framework to provide excellent prognostics performance also for units that exhibited very dissimilar operating conditions compared to the operating conditions of units used for training the algorithms. Therefore, the proposed hybrid framework sets a promising direction for further research in PHM applications.

As discussed earlier, solely feed-forward neural networks have been applied in this research. The development of time-dependent deep learning architectures, such as recurrent neural networks or convolutional neural networks within the hybrid prognostics framework has the potential to provide an additional performance improvement and should be explored further.

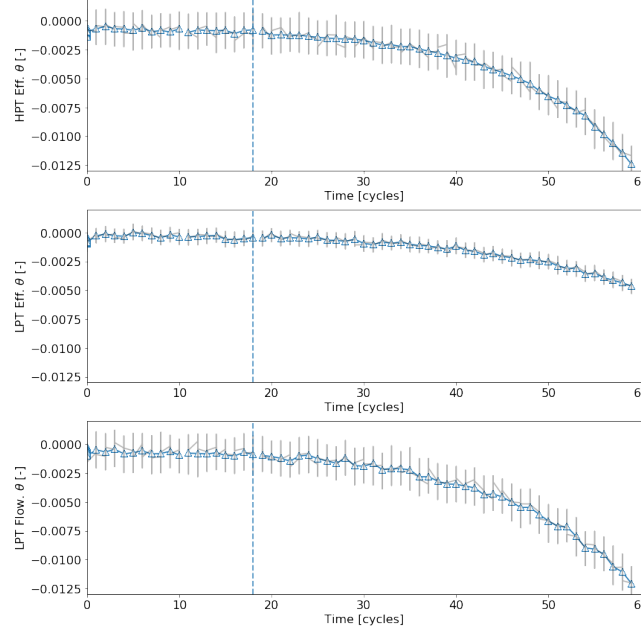


Figure 10: Calibration factors for a noise level of  $\text{SNR}_{db} = 20$  (grey) imposed on the high pressure turbine (HPT) efficiency, low pressure turbine (LPT) efficiency and flow for unit 11. The cycle of transition from *normal degradation* to *abnormal degradation* is indicated by the dotted vertical line.

Finally, a further potential future research direction is the evaluation of the transferability of the proposed hybrid approach to other types of problems that fulfil the same criteria: availability of complete physics-based models and the availability of sensor reading that provide information about the system state.

## Acknowledgements

This research was funded by the Swiss National Science Foundation (SNSF) Grant no. PP00P2 176878.

## References

- [1] Matthew J Daigle and Kai Goebel. A Model-Based Prognostics Approach Applied to Pneumatic Valves. *International Journal of Prognostics and Health Management*, 2:1–16, 2011.
- [2] Matthew J. Daigle and Kai Goebel. Model-based prognostics with concurrent damage progression processes. *IEEE Transactions on Systems, Man, and Cybernetics Part A: Systems and Humans*, 43(3):535–546, may 2013.
- [3] Mark Schwabacher and Kai Goebel. A survey of artificial intelligence for prognostics. *Association for the Advancement of Artificial Intelligence AAAI Fall Symposium 2007*, pages 107–114, 2007.
- [4] Samir Khan and Takehisa Yairi. A review on the application of deep learning in system health management, 2018.
- [5] Pankaj Malhotra, Vishnu TV, Anusha Ramakrishnan, Gaurangi Anand, Lovekesh Vig, Puneet Agarwal, and Gautam Shroff. Multi-Sensor Prognostics using an Unsupervised Health Index based on LSTM Encoder-Decoder. In *1st ACM SIGKDD Workshop on Machine Learning for Prognostics and Health Management*, page 10, San Francisco, 2016.
- [6] Andre S Yoon, Taehoon Lee, Yongsub Lim, Deokwoo Jung, Philgyun Kang, Dongwon Kim, Keuntae Park, and Yongjin Choi. Semi-supervised Learning with Deep Generative Models for Asset Failure Prediction. In *KDD17 Workshop on Machine Learning for Prognostics and Health Management*, page 9, Halifax, 2017.
- [7] Rui Zhao, Ruqiang Yan, Jinjiang Wang, and Kezhi Mao. Learning to monitor machine health with convolutional Bi-directional LSTM networks. *Sensors (Switzerland)*, 2017.
- [8] Xiang Li, Qian Ding, and Jian-Qiao Sun. Remaining useful life estimation in prognostics using deep convolution neural networks. *Reliability Engineering & System Safety*, 172:1–11, apr 2018.

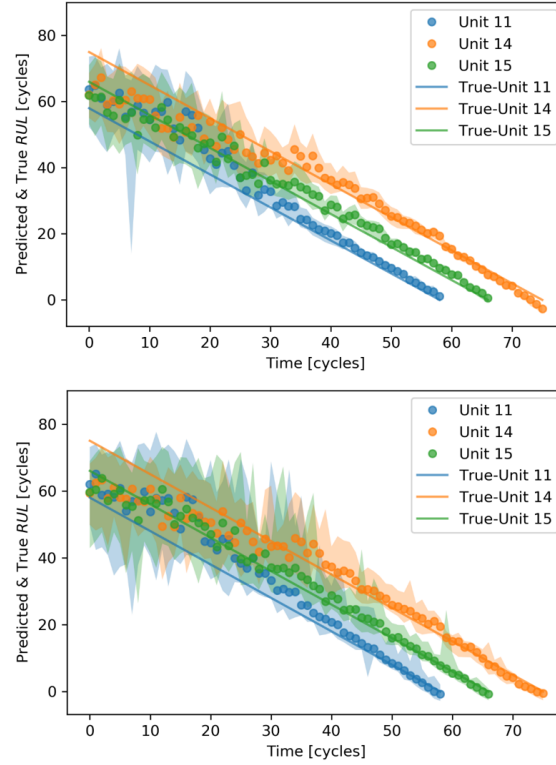


Figure 11: True and predicted  $RUL$  of the proposed hybrid approach with noisy calibration factors for noise levels of  $SNR_{db} = 30$  (top) and  $SNR_{db} = 10$  (bottom) imposed on the high pressure turbine (HPT) efficiency, low pressure turbine (LPT) efficiency for each unit. True and predicted  $RUL$  of the baseline model (top) and the proposed hybrid approach (bottom) for each test unit. The full lines correspond to the true  $RUL$ , the dotted lines are the average  $RUL$  estimate at each cycle i.e.  $\hat{y}_u^{[c]}$  and the shaded surface is the variability of the  $RUL$  predictions within each cycle. The upper limit corresponds to  $\max(\hat{y}_u^{[c]})$  and the lower bound is  $\min(\hat{y}_u^{[c]})$ . The three test units are shown: Unit 11 (blue), Units 14 (orange) and Unit 15 (green).

- [9] Gabriel Duarte Pasa, Ivo Paixão de Medeiros, and Takashi Yoneyama. Operating Condition-Invariant Neural Network-based Prognostics Methods applied on Turbofan Aircraft Engines. *Proceedings of the Annual Conference of the PHM Society*, 11(1), sep 2019.
- [10] A. Agogino and Kai Goebel. Milling Data Set, 2007.
- [11] Abhinav Saxena and Kai Goebel. Turbofan Engine Degradation Simulation Data Set, 2008.
- [12] Linxia Liao and Felix Köttig. Review of hybrid prognostics approaches for remaining useful life prediction of engineered systems, and an application to battery life prediction. *IEEE Transactions on Reliability*, 2014.
- [13] Prashanth Pillai, Anshul Kaushik, Shivanand Bhavikatti, Arjun Roy, and Virendra Kumar. A Hybrid Approach for Fusing Physics and Data for Failure Prediction. *International Journal of Prognostics and Health Management*, pages 2153–2648, 2016.
- [14] Dong Zhang, Satadru Dey, Hector E Perez, and Scott J Moura. Remaining Useful Life Estimation of Lithium-Ion Batteries based on Thermal Dynamics. pages 4042–4047, 2017.
- [15] Renato Giorgiani Nascimento and Felipe A.C. Viana. Fleet prognosis with physics-informed recurrent neural networks. In *Structural Health Monitoring 2019: Enabling Intelligent Life-Cycle Health Management for Industry Internet of Things (IIOT) - Proceedings of the 12th International Workshop on Structural Health Monitoring*, volume 2, pages 1740–1747, 2019.
- [16] Arinan Dourado and Felipe A. C. Viana. Physics-Informed Neural Networks for Corrosion-Fatigue Prognosis. *Proceedings of the Annual Conference of the PHM Society*, 11(1), sep 2019.

- [17] Yigit Anil Yucesan and Felipe A C Viana. Wind Turbine Main Bearing Fatigue Life Estimation with Physics-informed Neural Networks. In *Phm 2019*, volume 11, pages 1–14, 2019.
- [18] Xiaowei Jia, Anuj Karpatne, Jared Willard, Michael Steinbach, Jordan Read, Paul C Hanson, Hilary A Dugan, and Vipin Kumar. Physics Guided Recurrent Neural Networks For Modeling Dynamical Systems: Application to Monitoring Water Temperature And Quality In Lakes. Technical report, 2018.
- [19] Manuel Arias Chao, Chetan S Kulkarni, Kai Goebel, and Olga Fink. Hybrid deep fault detection and isolation: Combining deep neural networks and system performance models. *International Journal of Prognostics and Health Management*, 10:1–19, 2019.
- [20] Dean K Frederick, Jonathan A Decastro, and Jonathan S Litt. User’s Guide for the Commercial Modular Aero-Propulsion System Simulation (C-MAPSS). Technical report, 2007.
- [21] DASHlink - Flight Data For Tail 687, 2012.
- [22] Marc C. Kennedy and Anthony O’Hagan. Bayesian calibration of computer models. *Journal of the Royal Statistical Society: Series B (Statistical Methodology)*, 63(3):425–464, 2001.
- [23] Manuel Arias Chao, Darrel S. Lilley, Peter Mathé, and Volker Schloßhauer. Calibration and Uncertainty Quantification of Gas Turbine Performance Models. In *Proceedings of the ASME Turbo Expo*, volume 7A, page V07AT29A001, 2015.
- [24] Bryce A. Roth, David L. Doel, and Jeffrey J. Cissell. Probabilistic matching of turbofan engine performance models to test data. In *Proceedings of the ASME Turbo Expo*, volume 1, pages 541–548. American Society of Mechanical Engineers Digital Collection, nov 2005.
- [25] John L. Crassidis and John L. Junkins. *Optimal Estimation of Dynamic Systems, Second Edition (Chapman & Hall/CRC Applied Mathematics & Nonlinear Science)*. Chapman & Hall/CRC, 2nd edition, 2011.
- [26] S.J Borguet. *Variations on the Kalman Filter for Enhanced Performance Monitoring of Gas Turbine Engines*. Phd thesis, Université de Liège, 2012.
- [27] Nikolas Kantas, Arnaud Doucet, Sumeetpal S Singh, Jan Maciejowski, and Nicolas Chopin. On Particle Methods for Parameter Estimation in State-Space Models. *Statistical Science*, 30(3):328–351, 2015.
- [28] Simon J Julier and Jeffrey K Uhlmann. New extension of the Kalman filter to nonlinear systems. In *Signal Processing, Sensor Fusion, and Target Recognition VI*, volume 3068, page 182, 1997.
- [29] Qin Wang, Gabriel Michau, and Olga Fink. Missing-class-robust domain adaptation by unilateral alignment. *IEEE Transactions on Industrial Electronics*, 2020.
- [30] Manuel Arias Chao, Chetan S Kulkarni, Kai Goebel, and Olga Fink. Damage propagation modeling for aircraft engine run-to-failure simulation under real flight conditions. *Under review*, 2020.
- [31] Diederik P Kingma and Jimmy Lei Ba. Adam: A method for stochastic optimization. In *3rd International Conference on Learning Representations, ICLR 2015 - Conference Track Proceedings*, 2015.
- [32] Xavier Glorot and Yoshua Bengio. Understanding the difficulty of training deep feedforward neural networks. Technical report, 2010.
- [33] Abhinav Saxena, Kai Goebel, Don Simon, and Neil Eklund. Damage propagation modeling for aircraft engine run-to-failure simulation. In *2008 International Conference on Prognostics and Health Management*, pages 1–9. IEEE, oct 2008.